

Electrically interfaced Brillouin-active waveguide for microwave photonic measurements

Received: 10 July 2023

Accepted: 23 July 2024

Published online: 09 August 2024

 Check for updates

Yishu Zhou¹✉, Freek Ruesink¹, Margaret Pavlovich¹, Ryan Behunin², Haotian Cheng¹, Shai Gertler¹, Andrew L. Starbuck³, Andrew J. Leenheer¹, Andrew T. Pomerene³, Douglas C. Trotter³, Katherine M. Musick³, Michael Gehl¹, Ashok Kodigala³, Matt Eichenfield¹, Anthony L. Lentine³, Nils Otterstrom³ & Peter Rakich¹✉

New strategies for converting signals between optical and microwave domains could play a pivotal role in advancing both classical and quantum technologies. Traditional approaches to optical-to-microwave transduction typically perturb or destroy the information encoded on intensity of the light field, eliminating the possibility for further processing or distribution of these signals. In this paper, we introduce an optical-to-microwave conversion method that allows for both detection and spectral analysis of microwave photonic signals without degradation of their information content. This functionality is demonstrated using an optomechanical waveguide integrated with a piezoelectric transducer. Efficient electromechanical and optomechanical coupling within this system permits bidirectional optical-to-microwave conversion with a quantum efficiency of up to -54.16 dB. Leveraging the preservation of the optical field envelope in intramodal Brillouin scattering, we demonstrate a multi-channel microwave photonic filter by transmitting an optical signal through a series of electro-optomechanical waveguide segments, each with distinct resonance frequencies. Such electro-optomechanical systems could offer flexible strategies for remote sensing, channelization, and spectrum analysis in microwave photonics.

The ability to exchange information between optical and microwave domains is crucial for classical and quantum signal processing, computing, communication, and networking. Optical-to-microwave conversion is conventionally performed with the use of a photodiode to convert intensity-modulated optical signals into rapidly oscillating photocurrents. However, this process leads to the complete absorption of optical photons, causing the irreversible loss of encoded information in the light field. As an alternative to photodetection, bidirectional transduction of signals between optical and microwave

domains has recently been demonstrated using electro-optic^{1,2}, magneto-optic³, and acousto-optic⁴ interactions. Since these transduction mechanisms do not destroy the incident optical photons, they could offer the potential to enable microwave photonic measurements without information degradation, which could permit further processing or distribution of optical signals following the detection process.

Among the different approaches to encode and decode radiofrequency (RF) signals imprinted on light, acousto-optical coupling is appealing since GHz frequency elastic waves and optical waves can be

¹Department of Applied Physics, Yale University, New Haven, CT, USA. ²Department of Applied Physics and Materials Science, Northern Arizona University, Flagstaff, AZ, USA. ³Microsystems Engineering, Science, and Applications, Sandia National Laboratories, Albuquerque, NM, USA. ⁴James C. Wyant College of Optical Sciences, University of Arizona, Tucson, AZ, USA. ✉e-mail: yishu.zhou@yale.edu; peter.rakich@yale.edu

confined in the same micro-scale structure to produce efficient coupling. For example, engineerable Brillouin scattering processes have been used to convert signals between optical and acoustic domains, enabling new chip-based microwave photonic functionalities such as microwave measurement⁵, synthesis^{6,7}, high-resolution filtering^{8–11}, and signal processing^{12,13}. In principle, once these optical signals are converted to the acoustic domain, they can be directly read out through electromechanical coupling in piezoelectric materials to achieve electro-optomechanical optical-to-microwave conversion. To date, studies of electro-optomechanical conversion have exploited cavity-optomechanical systems, which use optical cavities^{14–21} to enhance the bidirectional microwave-to-optical conversion efficiency. However, such cavity-based systems can only accept optical signals over a narrow optical bandwidth, and they typically alter the information encoded within the intensity envelope of the incident light, limiting the signal processing architectures one can consider.

Here, we introduce a microwave photonic measurement method that preserves information integrity, using a traveling wave electro-optomechanical system. This system is realized through an electrically interfaced Brillouin-active waveguide in silicon photonics, allowing for wideband optical operation and unique mode dynamics among optical, acoustical, and microwave waves. Enhancement of the electro-optomechanical coupling is produced only using acoustic resonance, yielding bidirectional optical-to-microwave conversion with a quantum efficiency of up to -54.16 dB. In contrast to previous systems that utilized interband scattering^{22,23}, our approach leverages intramodal scattering to maintain the intensity envelope of the incident optical field during the optical-to-microwave transduction process. Since information encoded within the intensity envelope remains unchanged during the measurement, this approach enables further processing and distribution of optical signals for applications including channelization and advanced remote sensing. As a proof of concept, we demonstrate a multi-channel microwave photonic signal analyzer by cascading several Brillouin-active waveguide segments with distinct resonance frequencies.

Results

Device design

The system under study is composed of a suspended AlN-on-silicon membrane with a silicon ridge waveguide at its center, as illustrated in Fig. 1a. The suspended membrane is enclosed by a phononic crystal, facilitating the confinement for a high-Q phonon mode at frequency $\Omega_0/(2\pi) \sim 3.64$ GHz. Simultaneously, the ridge waveguide provides optical confinement for a low-loss TE-like optical mode in telecom wavelengths. A pair of compact IDTs symmetrically flank the optical ridge waveguide, enabling the piezoelectric coupling to acoustic phonons. The dimensions of the structure (See “Methods”) are tailored to ensure large acousto-optic and electromechanical mode overlaps, thus yielding substantial acousto-optic scattering and electro-mechanical transduction. The entire system is fabricated using the CMOS foundry process reported in ref. 24.

The bidirectional operation schemes of the electrically interfaced Brillouin scattering are shown in Fig. 1b and c. In Fig. 1b, a microwave drive at frequency Ω_0 excites elastic waves towards the optical waveguide, with an acoustic wavevector $q=0$ in the z -direction. These phonons then interact with the light traveling in the optical waveguide via photoelastic scattering. In the presence of a strong phonon drive, incident light of frequency ω_0 scatters into several optical sidebands at frequencies $\omega_n = \omega_0 + n\Omega_0$ with n being an integer. This creates a comb-like optical spectrum. Conversely, as depicted in Fig. 1c, acoustic phonons can be generated by the optical force exerted through an intensity-modulated light field via photoelasticity, a process known as stimulated Brillouin scattering. These phonons then propagate through the membrane, resulting in the generation of a microwave signal output through the IDT transduction. Both processes induce a phase modulation on the incident light field through variations in the refractive index resulting from phonon-induced density and pressure fluctuations^{25,26}. Consequently, this system effectively maintains the amplitude of the incident optical field, ensuring the preservation of any information encoded within the light's intensity envelope. This amplitude-preserving characteristic has significant potential for

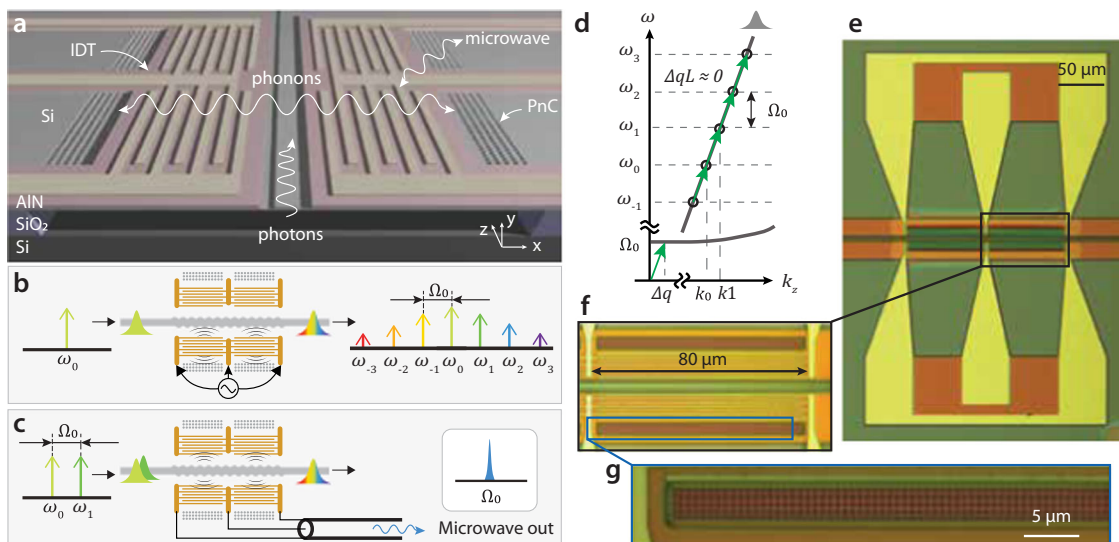


Fig. 1 | Layout and operation of the electrically interfaced Brillouin-active waveguide. **a** A 3D rendering of the device. The photons travel along the single-mode silicon ridge waveguide located in the center of the suspended membrane, while the phonons are confined laterally within the membrane by the phononic crystal structure on either side. Flanking the optical ridge waveguide is a pair of compact interdigitated transducers (IDTs), which enable the device to interface with microwave signals through piezoelectric transduction. **b, c** The bi-directionality of electrically interfaced Brillouin scattering process. The phonons

can either be electrically driven to produce an acousto-optical comb-like light spectrum (b), or optically excited to transduce the optical signal into a microwave signal via the IDTs (c). Both processes facilitate a phase modulation on the incident light, therefore preserving the optical intensity envelope. **d** The dispersion relations of the forward Brillouin scattering process. **e–g** Optical micrographs of the actual device, which was fabricated using a CMOS foundry process on an AlN-on-SOI platform.

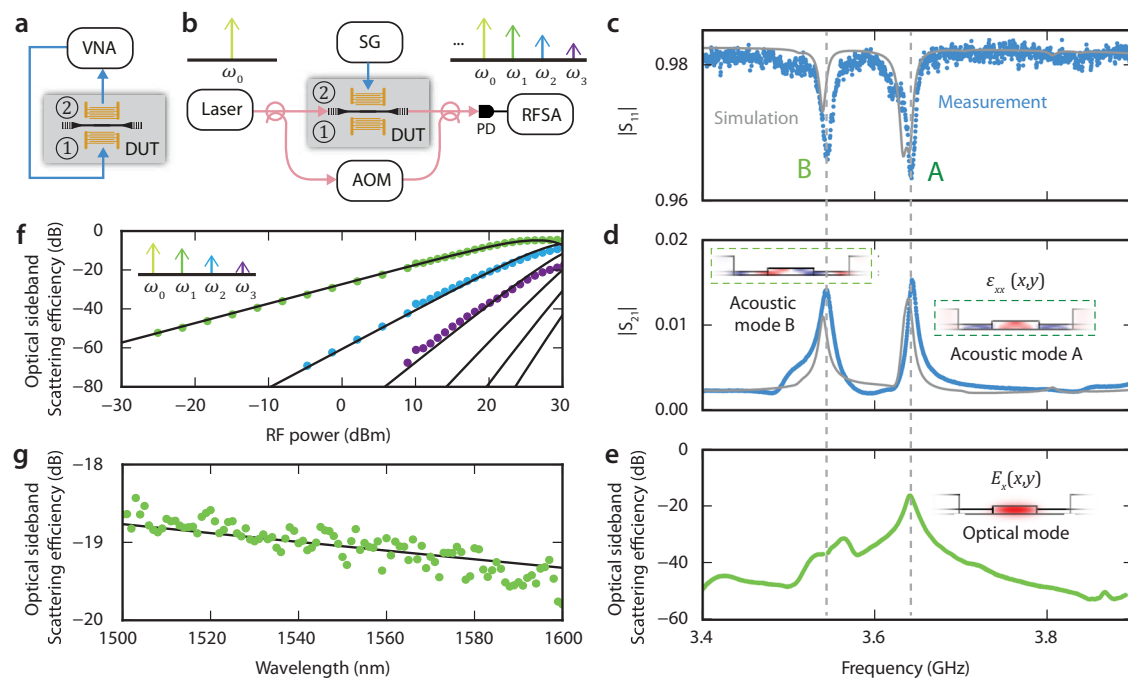


Fig. 2 | Electro-optomechanical phase modulation. **a** The experimental setup for electrical characterization. VNA: vector network analyzer. **b** A heterodyne setup to characterize electro-optomechanical phase modulation. SG: signal generator, AOM: acousto-optic modulator, RFSA: RF spectrum analyzer. Microwave reflection $|S_{11}|$ **(c)** and transmission $|S_{21}|$ **(d)** of the IDTs, obtained from experimental measurements (blue) and finite-element simulations (grey). These traces reveal two distinct electromechanical resonances corresponding to modes A and B, with detailed mode profiles shown as insets in **(d)**. **e** The first optical sideband measurement by sweeping the driving RF frequency obtained using the setup shown in

(b). The scattering efficiency, defined as the conversion efficiency of the 1st sideband $|a_1|^2/|a_0|^2$, is proportional to the mode overlaps between the acoustic (**(d)** inset) and optical (**(e)** inset) modes. As a result, mode A exhibits significantly stronger modulation efficiency compared to mode B. **f** RF power sweep of scattering efficiency of first three sidebands at mode A, which closely follows the theoretical predictions of Bessel functions. We obtain a $V_n = 8.13$ V and $V_n L = 0.13$ V cm. **g** Scattering of the first sideband shows minimal variation over a wavelength range of 100 nm. The measurement is taken under the RF drive of 8.92 dBm.

diverse applications in microwave photonic technologies, aspects of which will be further explored in this paper.

The phase-matching diagram in Fig. 1d suggests that to achieve maximum efficiency in Brillouin scattering, we need a wavevector of $q' = k_1 - k_0 = \Omega_0/v_g$. Although there is a small wavevector mismatch, Δq , between this ideal wavevector and the electrically driven phonon wavevector $q = 0$, the short interaction length of our device provides a negligible phase-mismatch $\Delta q L \ll 1$. Figure 1e–g depicts micrographs of a fabricated device, which consists of an acousto-optic interaction region that is 160 μm in length, along with two 2-IDT-units probed in a GSG (Ground/Signal/Ground) configuration. Figure 1g offers a magnified view of the phononic crystal region, characterized by a cubic lattice of air holes. In this study, we will demonstrate that our device is capable of efficient acousto-optical phase modulation and enables bidirectional conversion of signals between microwave and optical domains.

Electro-optomechanical phase modulation

Before delving into the microwave photonic measurements, it is essential to first understand this device's behavior. We begin by characterizing its operation under an electrical drive, where electrically induced acoustic waves lead to phase modulation of the incident light. Our characterization consists of two primary analyses: 1) Microwave Characterization (Fig. 2a), using a calibrated vector network analyzer (VNA) with two RF probes to measure all four S parameters of a pair of IDTs; and 2) Optical Scattering Characterization (Fig. 2b), where we examine the scattered optical sidebands of a monochromatic optical field through heterodyne measurement while electrically driving IDT 2. The measurement results for a 7-tooth IDT device, named Device 1, are presented in Fig. 2, with detailed parameters available in Table 1, “Methods”.

The frequency-dependent microwave reflection of IDT 1 ($|S_{11}|$) and microwave transmission from IDT 1 to IDT 2 ($|S_{21}|$) are shown in blue in Fig. 2c and d, aligning well with the simulated frequency-domain response obtained from COMSOL finite element analysis, shown in gray. Our measurements reveal two distinct electro-mechanical resonances in both the $|S_{11}|$ and $|S_{21}|$ measurements, namely mode A (3.64 GHz) and mode B (3.53 GHz), with the strain profiles shown in the insets of Fig. 2d. Despite a large impedance mismatch to the driving circuit caused by the compact IDT design, the IDT demonstrates appreciable electro-acoustic transduction efficiency, which is improved $\sim 4\times$ relative to a reference IDT without external acoustic resonances (Supplementary Information Sec. 3).

The acousto-optic coupling rate g , proportional to the mode overlap integral between the optical and acoustic modes, is primarily determined by the x -direction component, where the TEO-like optical mode features dominant displacement. Therefore, it is important to match the symmetry of the strain profile ϵ_{xx} (shown in the insets of Fig. 2d) with the optical mode profile E_x (shown in the inset of Fig. 2e). Here, mode A exhibits a symmetric strain component that is consistent with the symmetric optical mode, leading to much stronger acousto-optic scattering compared to the anti-symmetric strain profile observed in mode B. The quantified simulations of the acousto-optic scattering coefficient g of the driven acoustic modes can be referred to in Sec. 2.B of the Supplementary Materials.

We verify our simulation results by measuring the corresponding scattered optical sidebands of a monochromatic incident optical field with frequency ω_0 and amplitude a_0 . The amplitude of these sidebands can be obtained from the Bessel decomposition of the phase-

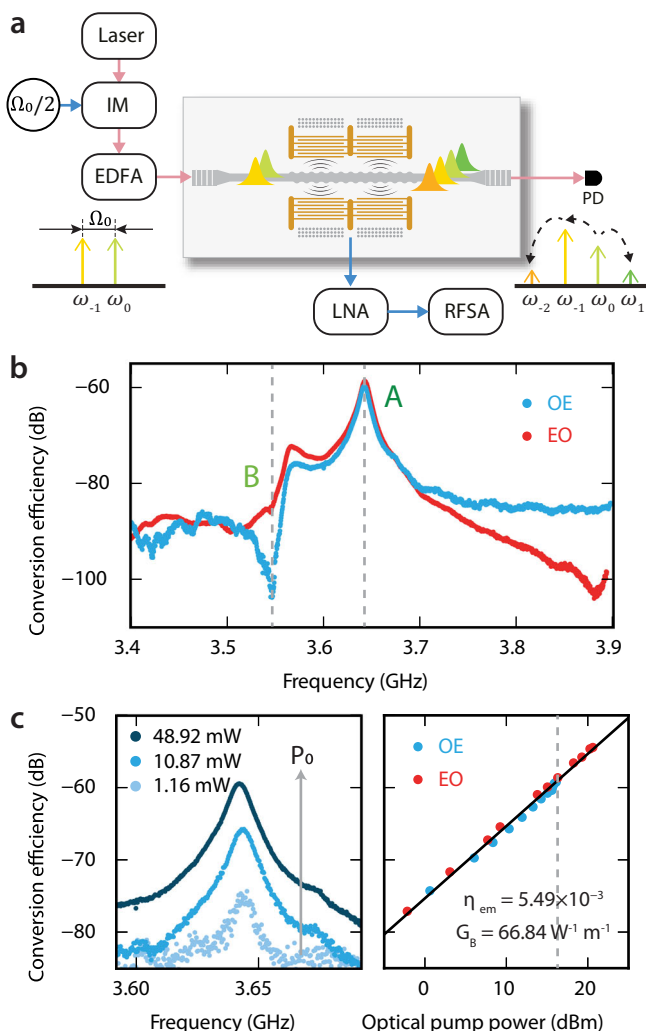


Fig. 3 | Bidirectional conversion. **a** Experimental setup for characterizing the optical-to-microwave conversion using a dual-drive configuration. LNA: low noise amplifier. **b** The quantum efficiency of optical-to-microwave conversion characterized at an optical pump power of 16.12 dBm (blue) and microwave-to-optical conversion characterized at an optical pump power of 16.32 dBm (red), with the peak transduction corresponding to mode A. **c** The peak of the optical-to-microwave conversion spectra at three different optical powers (left), along with an optical pump power sweep for both the optical-to-microwave (blue) and microwave-to-optical (red) conversions (right). The linear fitting (black) suggests a decent value of Brillouin gain G_B . The dashed line shows the optical pump power used in (b).

modulated optical output field as (Supplementary Information Sec. 1)

$$\tilde{a}_n(L, t) = t^n a_0 J_n(-\beta) e^{-i n \Omega_0 t}, \quad (1)$$

where the rotating frame $\tilde{a}_n(L, t) = a_n(L, t) e^{i \omega_0 t - i k_0 L}$ is introduced. The modulation depth, $\beta = 2|b|L/v_g$, where v_g is the group velocity of the optical mode, is determined by $|b|$, the phonon amplitude, which is controlled using the microwave drive. Consequently, the scattering efficiency of the n th sideband, calculated as $|a_n|^2/|a_0|^2$, is a function of both the microwave drive frequency and power.

In Fig. 2e, we present the scattering efficiency of the first sideband as a function of the microwave drive frequency, at a microwave drive power of 8.92 dBm. As expected, the optical scattering efficiency reaches its maximum of -16.32 dB at 3.64 GHz (mode A), indicating strong electromechanical Brillouin scattering. Conversely, due to opposing symmetries of the optical and acoustic modes, mode B

exhibits a dip in the measured spectrum, leading to a significantly lower scattering efficiency than mode A, with a decrease of over 20 dB. We also examine the dependence of scattering efficiency on RF power in Fig. 2f. We observe that the scattering efficiency at mode A for the first three sidebands aligns well with the theoretical predictions from Bessel functions in black. Overall, our compact optically-nonresonant system serves as a significant phase modulator with an effective half-wave voltage $V_n = 8.13 \pm 0.48$ V and $V_n L = 0.1301 \pm 0.0077$ V·cm. Note that the higher-order frequency tones ($n > 3$) are also present in this system as shown by the black curves in Fig. 2f. These tones are not measured because they fall outside the frequency range of our fast photodetector (Nortel PP-10G).

The absence of an optical cavity also enables wideband operation of our acousto-optic phase modulator, which is characterized in Fig. 2g. We characterize the first sideband scattering efficiency under the RF drive of 8.92 dBm, which shows <1 dB variation over 100 nm wavelength range. The measured efficiency follows a dominant $1/\lambda^2$ trend as denoted by the black line, which is caused by the phase-mismatch change at different optical wavelengths²⁷.

Bidirectional conversion

In addition to electrically driven optomechanical scattering, appreciable electro-optomechanical coupling permits the system to operate in reverse, allowing for optical-to-microwave conversion. This forms the foundation of our optical envelope preserving microwave photonic measurements.

The optical-to-microwave conversion process is investigated through a dual-drive stimulated Brillouin process, as illustrated in the setup depicted in Fig. 3a. Two drive fields, each with equal powers ($P_0 = P_{-1}$), are produced: one is a pump drive at frequency ω_0 , and the other is a Stokes drive at frequency ω_{-1} . These drives are generated using a carrier-suppressed intensity modulator, driven at a frequency of $\Omega_0/2$. As these optical fields propagate through the optical linear waveguide, the optical beat note between the fields generates a time-modulated optical force. This force transduces phonons at frequencies near the Brillouin frequency, Ω_0 . These optically driven phonons, in turn, facilitate energy transfer between the optical fields through a nonlinear optical process known as stimulated Brillouin scattering. As the phonons propagate throughout the membrane structure and interact with the IDTs, they are piezoelectrically converted into microwave photons.

The Brillouin gain coefficient, G_B , can be used to succinctly describe the efficiency of this conversion process. The generated phonons scatter the pump field into the Stokes field, increasing the Stokes power as $dP_{-1}/dz = G_B P_0 P_{-1}$, with G_B being the Brillouin gain coefficient. Since the production of each phonon coincides with the production of a Stokes photon, we can identify the phonon generation rate as $R_b = G_B P_0 P_{-1} L / (\hbar \omega_0)$. Hence, the quantum efficiency of converting the incoming flux of guided signal photons into microwave photons is calculated as

$$\eta = \frac{1}{2} \eta_{em} G_B P_0 L. \quad (2)$$

Here, η_{em} is the external electromechanical coupling factor that describes the efficiency with which a phonon in the membrane is converted to a microwave photon exiting the microwave probe. We also show that this same equation for quantum efficiency, η , is obtained when analyzing the efficiency of microwave-to-optical conversion (Supplementary Information Sec. 1). Hence, η describes the efficiency of bidirectional conversion within this system. Interestingly, this conversion efficiency is reminiscent of traditional cavity electro-optomechanical systems, $\eta = \eta_{em} \eta_{om} \frac{4C_{om}}{1+C_{om}^2}$, in the limit when $C_{om} \gg G_B P_0 L / 4 \ll 1$ ^{28,29}. Here, η_{om} describes the external coupling factor of the optomechanical system and is equal to 1, as all the

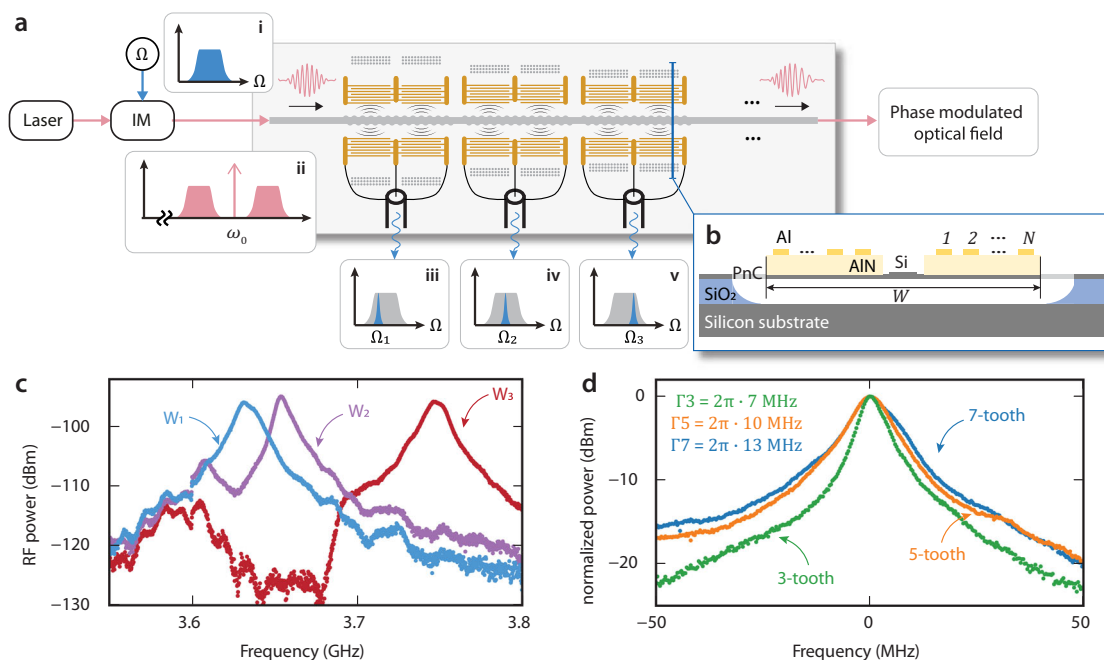


Fig. 4 | Microwave photonic channelization. **a** Operating principle of a multi-segment electrically interfaced Brillouin-active waveguide for microwave photonic channelization. Intensity-modulated light (ii) carrying a wideband RF signal (i) is injected into the system, which excites localized phonons at each electro-optomechanical region. Each phonon generates a microwave signal output with a designed center frequency and targeted bandwidth (iii–v). Despite undergoing several phase modulations, the output optical field preserves the intensity

envelope, ensuring that the RF information encoded in the optical signal remains unaltered. **b** The cross-section of the Brillouin-active waveguide, illustrating the membrane width W and the number of IDT teeth N . **c** Tunability of the microwave filter center frequency using the membrane width (W) of $W_1 = 14.70 \mu\text{m}$, $W_2 = 15.43 \mu\text{m}$, and $W_3 = 16.15 \mu\text{m}$. **d** Tunability of the microwave filter bandwidth using the number of IDT teeth.

photons can directly transit through our optical linear waveguide with negligible losses. Moreover, the factor of $\frac{1}{2}$ in Eq. (2) arises from the presence of two IDTs: microwave energy is emitted by each IDT into two microwave output ports, and we only detect the microwave energy from one of these ports.

Figure 3 b (Supplementary Data 1) shows the frequency-dependent measurement of the conversion efficiency of another 5-tooth IDT device, named Device 2 (for device parameters, see “Methods”). The measured microwave-to-optical conversion efficiency (EO) at an RF power of 8.92 dBm and an optical pump power of 16.32 dBm are shown in red, while the optical-to-microwave conversion efficiency (OE) measured with an optical pump power and an optical signal power both set at 16.12 dBm are shown in blue. Both curves exhibit similar peak conversion efficiencies of approximately -59 dB at 3.64 GHz, corresponding to acoustic mode A as shown in Fig. 2d. We note that the OE measurement shows a significant cancellation dip at mode B, which corresponds well to the nullified acousto-optic coupling rate as discussed in the electro-optomechanical phase modulation section.

To further understand the system properties, we performed an optical pump power sweep as shown in Fig. 3c. The left panel displays the zoomed-in frequency sweeps of the optical-to-microwave efficiency at different optical power levels, namely 116 mW, 10.87 mW, and 48.92 mW. The negligible change in the Lorentzian shape of the spectra suggests that the system experiences minimal thermo-optic heating, demonstrating the advantage of employing a linear waveguide system. This capability for handling large optical power enable high dynamic range applications in sensing and communication. The right panel exhibits the well-aligned quantum efficiency of both the optical-to-microwave (blue) and microwave-to-optical (red) conversions as a function of optical pump power. By increasing the optical pump power, we measured the maximum EO efficiency to be -54.16 ± 0.24 dB, highlighting the efficient operation of our device.

Note that these efficiencies are calculated for extrinsic conversion between the off-chip RF power and the on-chip optical power, including the IDT impedance mismatch loss but excluding the fiber-chip coupling loss. The exclusion of the fiber-chip coupling loss, approximately -6.5 dB per facet, is due to the device’s design for integration with other on-chip optical components, which will be discussed in the section of microwave photonic channelization. Calculating the microwave photons converted inside the IDTs, the maximum on-chip EO quantum efficiency can reach up to -31.56 ± 0.24 dB. Considering the measured electromechanical coupling factor of $\eta_{\text{em}} = 5.49 \times 10^{-3}$, we determine a Brillouin gain of $G_B = 66.84 \pm 3.63 \text{ W}^{-1} \cdot \text{m}^{-1}$ through linear fitting (black line). Notably, it should be acknowledged that this value is approximately four times smaller than our COMSOL simulations. This discrepancy may arise from fabrication imperfections, suboptimal acousto-optical overlaps, and reduced photoelastic constants of strained silicon, which indicates significant room for improvement in our device (Supplementary Information Sec. 2.B).

Microwave photonic channelization

This form of optical-to-microwave conversion is an intriguing alternative to fast photodetectors as a passive and non-disturbing means of extracting the microwave signal encoded on light (See Supplementary Information Sec. 6 for detailed discussion of photodiodes and our system). The intramodal Brillouin scattering generates phonons that only modulate the phase, not the intensity, of light. Therefore, information encoded on the intensity envelope of the light field is preserved (Supplementary Information Sec. 1). This principle allows for the construction of a microwave photonic channelizer by cascading Brillouin-active waveguide segments with distinct Brillouin frequencies, as illustrated in Fig. 4. Each segment transduces microwave signals at different frequencies while preserving the encoded intensity information.

The operation scheme of the multi-channel device is diagrammed in Fig. 4a. A sequence of electro-optomechanical regions is arranged along one linear waveguide, each supporting a distinct acoustic eigenmode with resonant frequency Ω_n and linewidth Γ_n . These properties can be adjusted through the geometric features of each region, such as the membrane width W and the number of IDT teeth, providing flexibility and tunability in the device design. A wideband RF signal (Fig. 4a.i) is encoded in the optical carrier (frequency ω_0) through intensity modulation, generating a light field with optical spectrum depicted in Fig. 4a.ii. The modulated light is then injected into the waveguide and excites localized phonons at a different frequency in each section, resulting in precise narrowband microwave readouts in each channel (Fig. 4a.iii to v). These optically driven phonons will each generate a pure phase modulation on the incident optical signal, resulting in an output field given as $a_{\text{out}} = a_{\text{in}} \exp[-i \sum_n \beta_n \cos(\Omega_n t)]$ (Supplementary Information Sec. 1). Here β_n is the modulation depth of the n th section, determined by the acoustic properties of the n th membrane. This implies that the original signal, the wideband RF signal injected into the intensity modulator, remains unchanged regardless of the presence of various Brillouin nonlinear interactions of different strengths and frequencies.

To experimentally validate the channelization concept, we measured a multi-channel device, with each active segment measuring 160 μm in length and separated by 130 μm . The filtering function of each channel can be individually tuned by the electrically interfaced Brillouin-active waveguide design in each channel, such as the membrane width (W) and the number of IDT teeth (N), as depicted in the cross-section in Fig. 4b. We controlled the center frequency of each filtering channel by adjusting the membrane width, as shown in Fig. 4c. Specifically, the transduced RF signal is measured from three segments with membrane widths of 16.15 μm , 15.43 μm , and 14.70 μm , corresponding to center frequencies of 3.746 GHz, 3.654 GHz, and 3.631 GHz, respectively. These measurements were taken using three 3-tooth IDT devices, named Device 4 to Device 6 with the parameters listed in “Methods”, providing similar transduction efficiency across all channels.

In our device, the major source of acoustic loss is metal scattering, making N , the number of IDT teeth a direct candidate for tuning the device’s bandwidth. Fig. 4d illustrates the characterization of active segments with 3, 5, and 7 IDT teeth, indicating a range of filtering bandwidths from 7 MHz to 13 MHz and demonstrating the design flexibility of the proposed method.

In summary, we successfully developed a microwave channelizer featuring tunable center frequency and filtering bandwidth for each channel. The feasibility of our proposal is grounded in the low-loss optical waveguide and compact form factor of each active segment. In our current setup, the optical propagation loss is negligible, making it possible to cascade 100 channels while maintaining minimal total propagation loss and acceptable phase-mismatch loss (Supplementary Information Sec. 2). As we consider larger systems, it is also interesting to note that the primary noise source, produced by spontaneous Brillouin scattering, also only impacts the phase information encoded on the optical wave. Hence, Brillouin scattering produced by this intramodal scattering process does not degrade the information encoded on the intensity of the light field.

Discussion

We use an electrically interfaced Brillouin-active waveguide to demonstrate an intriguing microwave photonic measurement method that maintains the information encoded in the optical intensity envelope. Leveraging the unique intensity envelope preserving dynamics of intramodal Brillouin scattering, we develop a microwave photonic channelizer in a tapped signal processing architecture through the cascading integration of these waveguide-based transducers. While further work is required to reach the high transduction

efficiencies ($\eta \sim 0.1$) and small half-wave voltages ($V_n \sim 19 \text{ mV}$) demonstrated using resonator-based systems³⁰, the target applications for these approaches are likely to be very different. For example, the high optical power-handling capability ($>100 \text{ mW}$) and broad bandwidths of optical transduction ($\sim 100 \text{ nm}$) produced by this waveguide system open the door to new schemes for high dynamic range microwave photonic signal processing. Furthermore, the system’s entirely passive operation, combined with its tapped architecture and signal processing capabilities, significantly simplifies complex setups. This is achieved by reducing reliance on biased photodiodes and power-hungry amplifiers, and by minimizing the need for additional RF filters. Such simplification makes the system particularly suitable for potential applications in remote sensing, where access to these components is often limited. Additionally, the small device footprint and CMOS compatibility of this fabrication process bode well for future scalability of such technologies.

To further enhance the electromechanical transduction efficiency η_{em} of this system we can greatly improve electromechanical coupling to the Brillouin-active phonon mode. The microwave extinction $\eta_e = 1 - |S_{11}(\Omega)|^2$ of the electromechanical transducer, which characterizes the efficiency with which microwaves are converted to phonons, is currently $\sim 2\%$ due to the large impedance mismatch between the compact IDT design and the standard 50 Ω input impedance. Increasing the system’s impedance or changing to a stronger piezoelectric material such as LiNbO₃^{31,32} or AlScN could enhance the efficiency of this conversion up to 50 \times . Additionally, we must increase the conversion efficiency of the microwave energy into the target acoustic mode, given by $\eta_m = \eta_{\text{em}}/\eta_e \sim 0.27\text{--}0.41$. Optimizing the IDT and acoustic membrane design can improve this efficiency at least 3 \times (Supplementary Information Sec. 2).

Extending the device length is another way to improve the performance of our system since the transduction efficiency η is proportional to L . Even with the phase-mismatch loss, the optical propagation loss, and the changes in IDT impedance mismatch, the transduction efficiency η could still be improved by $\sim 10 \text{ dB}$ by simply elongating the interaction length (for a detailed discussion, see SI Sec. 2.C). Moreover, the current measured Brillouin gain G_B is lower than 1/4 of the simulated values, indicating significant potential for design improvement. Specifically, our simulations indicate that aligning the electromechanical resonance more closely with an acoustic mode exhibiting substantial acousto-optical coupling could significantly improve performance (Fig. S3 in Sec. 2.B of the SI). Combining these improvements paves the way for a device with $\eta > -16 \text{ dB}$.

These performance enhancements position our device as the basis for a scalable and versatile platform for optical-to-microwave conversion, one that preserves information encoded in the intensity of the light field. This advancement opens the door to a wide array of applications, including quantum and classical transduction and communication, microwave photonic spectral analysis, and advanced remote sensing.

Methods

Device design

All the devices under study share the same basic structure, as illustrated in Fig. 5, where the 200 nm-thick aluminum IDT electrodes sit on a piezoelectric 480 nm-thick AlN film supported by a silicon membrane structure. To ensure both vertical and lateral acoustic confinement, the AlN/Si membrane is suspended and bordered laterally by a phononic crystal structure composed of circular holes with a diameter (pitch) of 616 (800) nm to ensure lateral acoustic confinement. The IDT pitch, $\Lambda = 2.9 \mu\text{m}$, is carefully designed to optimize the electromechanical transduction of the target phonon at the frequency Ω_0 . The silicon optical waveguide has a width of 1.5 μm . The AlN film is discontinued on top of the silicon optical waveguide in the center of the device by 3.7 μm to minimize the optical loss. The membrane width

Table 1 | The device parameters

Device parameters	Device 1	Device 2	Device 3	Device 4	Device 5	Device 6
The number of IDT teeth ^a	7	5	3	3	3	3
Membrane width W (μm) ^a	28.48	22.68	16.88	16.15	15.43	14.70
d (μm) ^a	1.84	1.84	1.84	1.48	1.11	0.75
$\Omega_0/(2\pi)$ (GHz) ^b	3.644	3.642	3.655	3.746	3.654	3.631
$\Gamma_0/(2\pi)$ (MHz) ^b	12.65	10.24	7.39	/	/	/
Acoustic Q-factor ^b	288.01	355.66	494.59	/	/	/
$\eta_{e,1} = 1 - \mathcal{S}_{11}(\Omega_0) ^2$ ^b	2.92%	1.25%	0.78%	/	/	/
$\eta_{e,2} = 1 - \mathcal{S}_{22}(\Omega_0) ^2$ ^b	3.38%	2.12%	1.28%	/	/	/
$\eta_{\text{em}} = \mathcal{S}_{12}(\Omega_0) ^2$ ^b	0.0132	5.49×10^{-3}	2.69×10^{-3}	/	/	/
η_m ^{b, c}	0.419	0.337	0.270	/	/	/
$g(\Omega_0)$ (Hz $\cdot\sqrt{\text{m}}$) ^d	1269.06	1972.31	1939.06	/	/	/
v_g (m/s) ^d	8.33×10^7	8.33×10^7	8.33×10^7	/	/	/
Simulated G_B (W $^{-1} \cdot \text{m}^{-1}$) ^d	91.14	271.95	364.24	/	/	/
Measured G_B (W $^{-1} \cdot \text{m}^{-1}$) ^{b, e}	27.45 ± 1.60	66.84 ± 3.63	50.64 ± 1.47	/	/	/
Maximum measured η_{OE} (dB) ^f	-59.79 ± 0.25	-59.24 ± 0.24	-63.49 ± 0.13	/	/	/
Maximum measured η_{EO} (dB) ^{b, g}	/	-54.16 ± 0.24	/	/	/	/

Notice that the source of the parameters is indicated in the footnote. Additionally, the columns with slashes are either not measured or not discussed in this work.

^aDevice designs.

^bExperimental measurements.

^cObtained as $\eta_m = \eta_{\text{em}} / \sqrt{\eta_{e,1}\eta_{e,2}}$.

^dCOMSOL simulations.

^eDerived from the dual-drive optical-to-microwave transduction measurement.

^fThe maximum measured value of quantum efficiency for optical-to-microwave conversion. Measured at an optical pump power of 16.12 dBm.

^gThe maximum measured value of quantum efficiency for microwave-to-optical conversion. Measured at an optical pump power of 20.61 dBm.

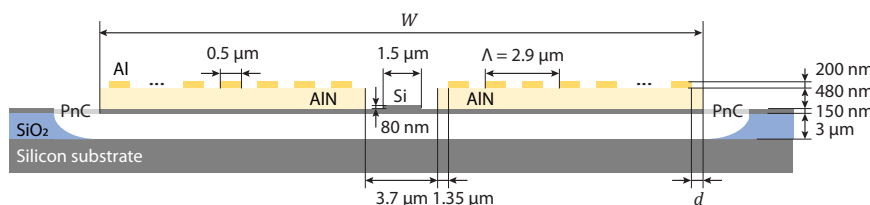


Fig. 5 | The basic device structure. Device 1 to Device 6 share similar structures but feature different parameters such as edge width (d) and number of teeth (N).

W , determined by the number of IDT teeth and the IDT to phononic crystal distance d , is used to adjust the acoustic resonance. In this paper, we studied one 7-tooth device (Device 1), one 5-tooth device (Device 2), and four 3-tooth devices (Device 3 to Device 6).

Device parameters

In the main text, we present measurements from six devices: Device 1 for the characterization of electromechanical Brillouin scattering and optical phase modulation (Figs. 2, 3), Device 2 for bidirectional optical-to-microwave transduction (Fig. 4), and Device 3 - 6 for the microwave channelization (Device 4, 5, 6 were measured in Fig. 5c and Device 1, 2, 3 were measured in Fig. 5d). We present the device designs, as well as their corresponding simulation and measurement results, in Table 1. Detailed analysis of these parameters is provided in Sec. 2 of the SI.

Data availability

Data sets generated during the current study are available from the corresponding author on request.

References

1. Rueda, A. et al. Efficient microwave to optical photon conversion: an electro-optical realization. *Optica* **3**, 597–604 (2016).
2. Hu, Y. et al. On-chip electro-optic frequency shifters and beam splitters. *Nature* **599**, 587–593 (2021).
3. Zhu, N. et al. Waveguide cavity optomagnonics for microwave-to-optics conversion. *Optica* **7**, 1291–1297 (2020).
4. McKenna, T. P. et al. Cryogenic microwave-to-optical conversion using a triply resonant lithium-niobate-on-sapphire transducer. *Optica* **7**, 1737–1745 (2020).
5. Jiang, H. et al. Wide-range, high-precision multiple microwave frequency measurement using a chip-based photonic Brillouin filter. *Optica* **3**, 30–34 (2016).
6. Li, J., Lee, H. & Vahala, K. J. Microwave synthesizer using an on-chip Brillouin oscillator. *Nat. Commun.* **4**, 2097 (2013).
7. Preußler, S. et al. Generation of ultra-narrow, stable and tunable millimeter-and terahertz-waves with very low phase noise. *Opt. Express* **21**, 23950–23962 (2013).
8. Stern, Y. et al. Tunable sharp and highly selective microwave-photonic band-pass filters based on stimulated Brillouin scattering. *Photonics Res.* **2**, B18–B25 (2014).
9. Marpaung, D. et al. Low-power, chip-based stimulated Brillouin scattering microwave photonic filter with ultrahigh selectivity. *Optica* **2**, 76–83 (2015).
10. Botter, R. et al. Guided-acoustic stimulated Brillouin scattering in silicon nitride photonic circuits. *Sci. Adv.* **8**, eabq2196 (2022).
11. Gertler, S. et al. Narrowband microwave-photonic notch filters using Brillouin-based signal transduction in silicon. *Nat. Commun.* **13**, 1947 (2022).

12. Choudhary, A. et al. Advanced integrated microwave signal processing with giant on-chip Brillouin gain. *J. Lightwave Technol.* **35**, 846–854 (2017).
13. Kim, H. et al. On-chip rf signal shaping by coherent control of optically driven acoustic wave interference. *ACS Photonics* **9**, 2938–2945 (2022).
14. Shao, L. et al. Microwave-to-optical conversion using lithium niobate thin-film acoustic resonators. *Optica* **6**, 1498–1505 (2019).
15. Han, X. et al. Cavity piezo-mechanics for superconducting-nanophotonic quantum interface. *Nat. Commun.* **11**, 3237 (2020).
16. Chu, Y. & Gröblacher, S. A perspective on hybrid quantum opto-and electromechanical systems. *Appl. Phys. Lett.* **117**, 150503 (2020).
17. Jiang, W. et al. Efficient bidirectional piezo-optomechanical transduction between microwave and optical frequency. *Nat. Commun.* **11**, 1166 (2020).
18. Mirhosseini, M., Sipahigil, A., Kalaee, M. & Painter, O. Superconducting qubit to optical photon transduction. *Nature* **588**, 599–603 (2020).
19. Hönl, S. et al. Microwave-to-optical conversion with a gallium phosphide photonic crystal cavity. *Nat. Commun.* **13**, 2065 (2022).
20. Stockill, R. et al. Ultra-low-noise microwave to optics conversion in gallium phosphide. *Nat. Commun.* **13**, 6583 (2022).
21. Yoon, T. et al. Simultaneous Brillouin and piezoelectric coupling to a high-frequency bulk acoustic resonator. *Optica* **10**, 110–117 (2023).
22. Liu, Q., Li, H. & Li, M. Electromechanical Brillouin scattering in integrated optomechanical waveguides. *Optica* **6**, 778–785 (2019).
23. Li, H., Liu, Q. & Li, M. Electromechanical Brillouin scattering in integrated planar photonics. *Appl. Photonics* **4**, 080802 (2019).
24. Zhou, Y., et al. Nonreciprocal dissipation engineering via strong coupling with a continuum of modes. *Phys. Rev. X* **14**, 021002 (2024).
25. Gorecki, C., Chollet, F., Bonnotte, E. & Kawakatsu, H. Silicon-based integrated interferometer with phase modulation driven by surface acoustic waves. *Opt. Lett.* **22**, 1784–1786 (1997).
26. Wolff, C., Stiller, B., Eggleton, B. J., Steel, M. J. & Poulton, C. G. Cascaded forward Brillouin scattering to all stokes orders. *N. J. Phys.* **19**, 023021 (2017).
27. Kittlaus, E. A. et al. Electrically driven acousto-optics and broadband non-reciprocity in silicon photonics. *Nat. Photonics* **15**, 43–52 (2021).
28. Otterstrom, N. T., Behunin, R. O., Kittlaus, E. A. & Rakich, P. T. Optomechanical cooling in a continuous system. *Phys. Rev. X* **8**, 041034 (2018).
29. Han, X., Fu, W., Zou, C.-L., Jiang, L. & Tang, H. X. Microwave-optical quantum frequency conversion. *Optica* **8**, 1050–1064 (2021).
30. Zhao, H., Li, B., Li, H. & Li, M. Enabling scalable optical computing in synthetic frequency dimension using integrated cavity acousto-optics. *Nat. Commun.* **13**, 5426 (2022).
31. Sarabalis, C. J., McKenna, T. P., Patel, R. N., Van Laer, R. & Safavi-Naeini, A. H. Acousto-optic modulation in lithium niobate on sapphire. *Appl. Photonics* **5**, 086104 (2020).
32. Wan, L. et al. Highly efficient acousto-optic modulation using nonsuspended thin-film lithium niobate-chalcogenide hybrid waveguides. *Light Sci. Appl.* **11**, 145 (2022).

Acknowledgements

We thank Yanni Dahmani, Taekwan Yoon, Betul Sen, and Naijun Jin for useful technical discussions involving Brillouin interactions and IDT designs. This research was developed with funding from the Defense Advanced Research Projects Agency (DARPA) under Award No. HR0011048577 and the National Science Foundation (NSF) under Award No. 2137740. The views, opinions, and/or findings expressed are those of the author and should not be interpreted as representing the official views or policies of the Department of Defense or the U.S. Government. Distribution Statement A - Approved for Public Release, Distribution

Unlimited. This material is based upon work supported by the Laboratory Directed Research and Development program at Sandia National Laboratories. Sandia National Laboratories is a multi-program laboratory managed and operated by National Technology and Engineering Solutions of Sandia, LLC., a wholly owned subsidiary of Honeywell International, Inc., for the U.S. Department of Energy's National Nuclear Security Administration under contract DE-NA-0003525. This paper describes objective technical results and analysis. The views, opinions, and/or findings expressed are those of the authors and should not be interpreted as representing the official views or policies of the U.S. Department of Energy, U.S. Department of Defense, or the U.S. Government.

Author contributions

Y.Z., F.R., and P.R. conceived the project. M.P. designed the devices with the assistance of S.G. Y.Z. conducted the experiments. Y.Z., R.B., and P.R. developed the theoretical models to describe the mode dynamics in the bidirectional microwave-to-optical process. Y.Z. and F.R. developed the analytical model to describe the resonant enhancement of electro-mechanical transduction. Y.Z. performed the numerical simulations with the assistance of H.C. A.L.S., A.J.L., A.T.P., D.C.T., K.M.M., M.G., A.K., M.E., A.L.L., and N.O. performed the silicon foundry fabrication at the Microsystems and Engineering Sciences Applications (MESA) facility, Sandia National Laboratory. Y.Z., F.R., and P.R. wrote the paper with the input from all authors. All authors contributed to the experiment design and discussion of the results.

Competing interests

The authors declare no competing interests.

Additional information

Supplementary information The online version contains supplementary material available at <https://doi.org/10.1038/s41467-024-51010-8>.

Correspondence and requests for materials should be addressed to Yishu Zhou or Peter Rakich.

Peer review information *Nature Communications* thanks the anonymous reviewer(s) for their contribution to the peer review of this work. A peer review file is available.

Reprints and permissions information is available at <http://www.nature.com/reprints>

Publisher's note Springer Nature remains neutral with regard to jurisdictional claims in published maps and institutional affiliations.

Open Access This article is licensed under a Creative Commons Attribution-NonCommercial-NoDerivatives 4.0 International License, which permits any non-commercial use, sharing, distribution and reproduction in any medium or format, as long as you give appropriate credit to the original author(s) and the source, provide a link to the Creative Commons licence, and indicate if you modified the licensed material. You do not have permission under this licence to share adapted material derived from this article or parts of it. The images or other third party material in this article are included in the article's Creative Commons licence, unless indicated otherwise in a credit line to the material. If material is not included in the article's Creative Commons licence and your intended use is not permitted by statutory regulation or exceeds the permitted use, you will need to obtain permission directly from the copyright holder. To view a copy of this licence, visit <http://creativecommons.org/licenses/by-nc-nd/4.0/>.

© The Author(s) 2024